Interfacial Water on Ag/Ag₂S Nanowires Enhancing the Ethanol Selectivity for CO₂ Electroreduction

Can-Jun Zou, Zi-Yu Du, Wei Tang, Qiong Liu, Xing-Biao Liu, Jin-Chao Dong, Ping-Ping Fang,* and Jian-Feng Li*

The electrochemical conversion of CO_2 into multicarbon products represents a pivotal yet challenging target, particularly for metal catalysts that predominantly yield C_1 products. Herein, this challenge is addressed through sulfur-induced electronic modulation of Ag-based catalysts, steering the CO_2 reduction pathway toward ethanol production. By constructing atomically engineered Ag/Ag₂S nanowires (NWs) via a controlled sulfurization strategy, a remarkable Faradaic efficiency (FE) of 75% for ethanol at −0.95 V, along with exceptional stability over 14 h of high-performance metrics surpassing most reported Ag-based systems is achieved. Operando electrochemical surface-enhanced Raman spectroscopy (EC-SERS) and density functional theory (DFT) calculations unveil that the Ag/Ag₂S heterointerface synergistically regulates interfacial water networks and stabilizes key *CO intermediates, thereby accelerating CO_2 activation, proton-coupled electron transfer, and asymmetric C-C coupling. Furthermore, sulfurization-induced dual effects-optimized hydrogen-bond interactions and enriched K^+ confinement are identified as critical drivers for tailoring the local microenvironment to favor ethanol selectivity. This work not only demonstrates a rational atomic interface design for C_2 product orientation but also deciphers the dynamic interplay between catalyst electronic structure and interfacial species, offering a molecular-level roadmap for advanced CO_2 conversion systems.

1. Introduction

CO_2 electroreduction to valuable fuels and chemicals, driven by clean electricity from renewable energy, presents an attractive route to achieve CO_2 utilization for alleviating the current energy crisis and greenhouse gas emissions.[1] Among various products, ethanol is highly desired because it is not only a commonly used industrial material but also a fuel with high energy density.[2] Yet it remains a great challenge to convert CO_2 to ethanol with high selectivity due to the low controllability over C-C coupling.[3] Silver (Ag) is reported to achieve high CO Faradaic efficiency (FE) exceeding 90% during CO_2 electroreduction.[4] Since CO is the key intermediate to realize C-C coupling to produce ethanol, strategies to further reduce CO on Ag-based catalysts have drawn increasing attention. Wang et al. reported the design of Ag^+-doped InSe nanosheets with Se vacancies which enables CO_2 electroreduction to a single liquid product of ethanol.[5] The heterointerface of Ag^+ and InSe promotes CO_2 activation and protonation via the synergistic stabilization of intermediates. We have found the partially oxidized Ag nanowires (NWs) can improve the ethanol selectivity via the enhanced *CO adsorption energy.[6] However, it is difficult to maintain both selectivity and durability on the naturally oxidized Ag surface experimentally, and there is a lack of clear definition for active sites mechanically. Ag/Ag₂S heterostructures can promote the CO_2 electroreduction activity and CO selectivity,[7] but how to modify Ag catalysts' interface using sulfur to improve the CO_2 electroreduction to C_2 products such as ethanol remains a significant challenge, while understanding mechanisms is even more challenging.

Investigation of mechanisms underlying CO_2 electroreduction requires real-time identification of dynamic interfacial species, particularly carbonaceous intermediates, and interfacial water. Detection of C_1 intermediates is crucial for elucidating the reaction mechanism at the initial stage.[8] In contrast, C_2 intermediates are more challenging to detect due to their lower surface coverage and transient nature, yet they offer deeper mechanistic insights, such as confirming the occurrence of C-C coupling and explaining the selectivity between ethanol and ethylene.[9]

C.-J. Zou, P.-P. Fang
School of Advanced Energy
Sun Yat-Sen University (Shenzhen)
Shenzhen 518107, China
E-mail: fangpp3@mail.sysu.edu.cn

Z.-Y. Du, J.-C. Dong, J.-F. Li
State Key Laboratory of Physical Chemistry of Solid Surfaces
iChEM
College of Chemistry and Chemical Engineering
College of Energy
College of Materials
Xiamen University
Xiamen 361005, China
E-mail: li@xmu.edu.cn

C.-J. Zou, W. Tang, Q. Liu, X.-B. Liu
School of Chemistry
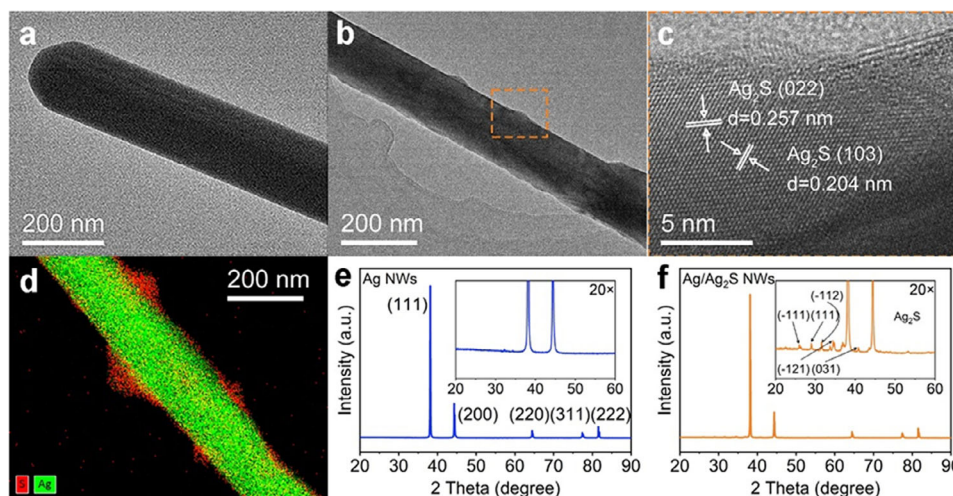Sun Yat-Sen University
Guangzhou 510275, China

Figure 1. TEM images of a) Ag NWs and b) Ag/Ag$_2$S NWs. c) High-resolution TEM images of Ag/Ag$_2$S NWs. d) EDS mapping image of Ag/Ag$_2$S NWs. XRD patterns and partially enlarged details of e) Ag NWs and f) Ag/Ag$_2$S NWs.

Despite its importance, interfacial water has been largely overlooked in previous studies, even though it plays an essential role in revealing the microenvironment during CO$_2$ electroreduction. For instance, Liu et al. found that the competitive adsorption of K$^+$ and *H revealed by interfacial water influences CO$_2$ electroreduction performance via the variations in local pH.[10] Wang et al. found that the optimized *H formation determined by strong hydrogen-bonded water leads to the balance between hydrogen evolution reaction (HER) and intermediate hydrogenation.[11] While optimal *H supply from interfacial water has been linked to promoted CO$_2$ electroreduction, its multifaceted roles, including hydrogen bonding and cation effects, merit further investigation.[10–13] Operando electrochemical surface-enhanced Raman spectroscopy (EC-SERS) has emerged as one of the powerful techniques for molecular fingerprint recognition during CO$_2$ electroreduction. Therefore, insights into intermediates and dynamic behaviors of interfacial water from EC-SERS allow for a more comprehensive reconstruction of the reaction process, thereby advancing our understanding of underlying mechanisms.

Herein, we systematically investigated how interfacial water, along with carbonaceous intermediates and the electronic structure of Ag/Ag$_2$S NWs influences ethanol selectivity and stability in CO$_2$ electroreduction by operando EC-SERS. Ag NWs with different sulfurized degrees were synthesized by adjusting the Na$_2$S concentration, with optimal ethanol selectivity of 75% achieved at a concentration of 10 mm. X-ray photoelectron spectroscopy (XPS) and density functional theory (DFT) calculations found such Ag/Ag$_2$S NWs exhibit the lowest binding energy of Ag3d and facilitate easier electron transfer to favor ethanol formation. Operando EC-SERS combined with DFT calculations identified the key intermediates and demonstrated how interfacial water facilitates C-C coupling and ethanol formation. This study explains why Ag/Ag$_2$S NWs exhibit high ethanol selectivity. The effects of K$^+$ and hydrogen bonding, mediated by interfacial water, enhance ethanol selectivity and provide valuable insights for designing catalysts with high ethanol selectivity.

2. Results

2.1. Characterization of Ag NWs and Ag/Ag$_2$S NWs

Transmission electron microscope (TEM), energy dispersive spectroscopy (EDS), and X-ray diffraction (XRD) were used to characterize Ag NWs and Ag/Ag$_2$S NWs. The width of Ag NWs is ≈180 nm and Ag$_2$S is distributed in the shape of an island on Ag NWs after sulfurization (**Figure 1a,b**). The sulfurized Ag can be clearly seen from the surface of Ag/Ag$_2$S NWs, while the lattice fringes of 0.257 and 0.204 nm are corresponded to Ag$_2$S(022) and Ag$_2$S(103) (Figure 1c). The EDS mapping image of Ag/Ag$_2$S NWs reveals a more distinct island-like distribution of Ag$_2$S, highlighting regions where both Ag$_2$S and Ag are exposed on the surface of Ag/Ag$_2$S NWs (Figure 1d). Scanning electron microscope (SEM) and TEM images further supported the uniformity of Ag/Ag$_2$S interfaces (Figures S1,S2, Supporting Information). XRD patterns of Ag NWs and Ag/Ag$_2$S NWs are shown in Figure 1e,f. The occurrence of a dozen small peaks between 20° and 60° including Ag$_2$S(−111), Ag$_2$S(111), Ag$_2$S(−112), Ag$_2$S(−121), and Ag$_2$S(031) on the XRD pattern in the partially enlarged detail further demonstrates the formation of Ag$_2$S on Ag NWs. Multiple batches of synthesis confirmed the reproducibility of Ag NWs and Ag/Ag$_2$S NWs by TEM, UV–vis spectroscopy, XRD, and XPS across multiple batches (Figures S2–S6, Supporting Information). Synthesis formulas, SEM images, and XRD patterns of Ag NWs with different sulfurization degrees are given in Supporting Information (Table S1, Figures S7,S8, Supporting Information).

2.2. Selectivity and Stability of Ag/Ag$_2$S NWs for CO$_2$ Electroreduction

CO$_2$ electroreduction behavior of Ag NWs and Ag/Ag$_2$S NWs was investigated by linear sweep voltammetry (LSV) (**Figure 2a**) and cyclic voltammetry (CV) (Figure S9, Supporting Information). The voltammetry curves were normalized based on the mass of Ag as determined by an inductively coupled plasma
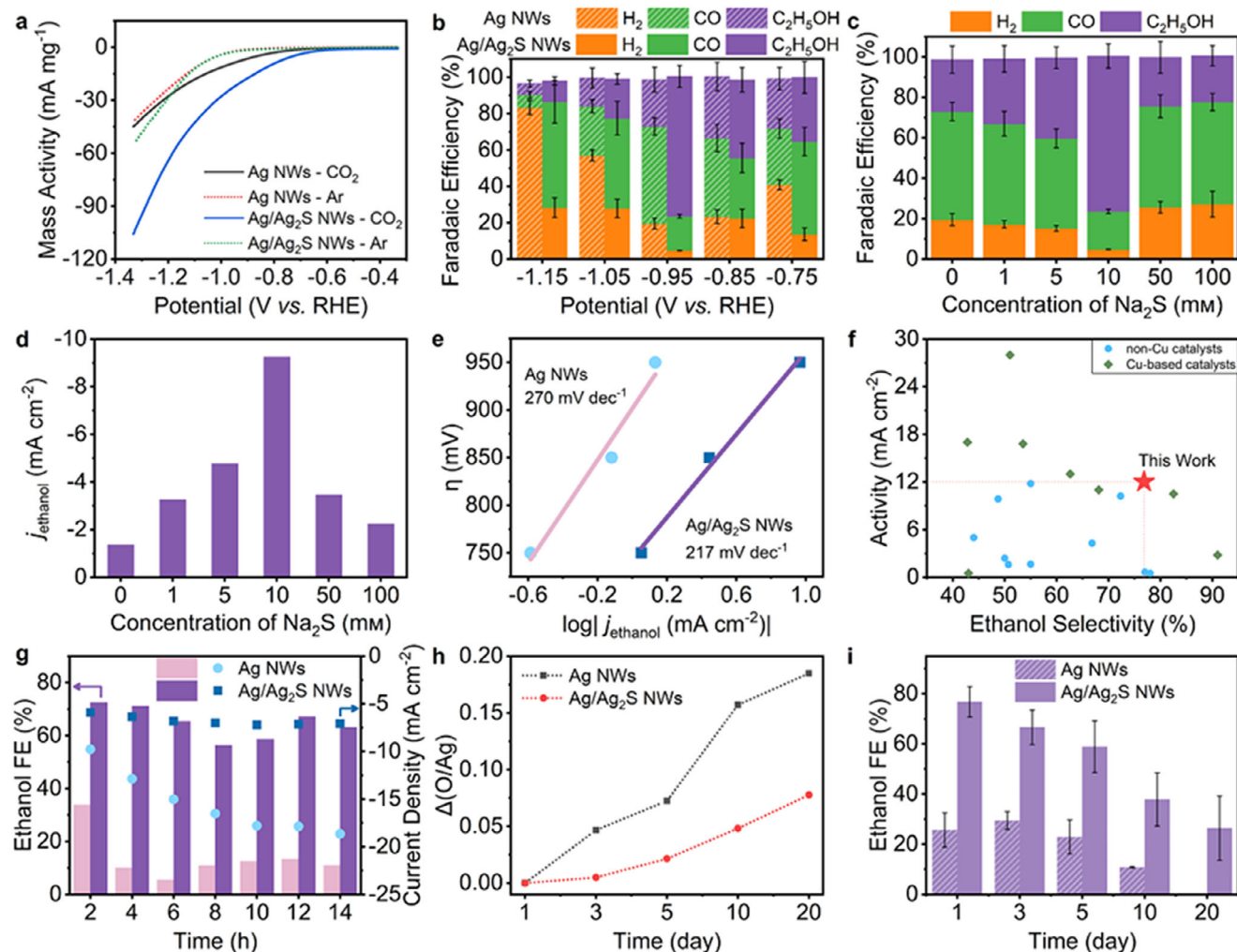
**ADVANCED
SCIENCE NEWS**

www.advancedsciencenews.com

**ADVANCED
MATERIALS**

www.advmat.de

Figure 2. a) LSV curves of Ag NWs and Ag/Ag$_2$S NWs in CO$_2$-saturated or Ar-saturated 0.5 M KHCO$_3$ solution. b) FE of different products during CO$_2$ electroreduction on Ag NWs and Ag/Ag$_2$S NWs. c) FE of different products during CO$_2$ electroreduction on Ag NWs with different sulfurization degrees at −0.95 V versus RHE. d) $j_{ethanol}$ of Ag NWs and Ag NWs with different sulfurization degrees. e) Tafel slope corresponding to $j_{ethanol}$ of Ag NWs and Ag/Ag$_2$S NWs. f) Comparison of activity and ethanol FE for reported catalysts in an H-type cell. g) Ethanol FE and current density during long-term electrolysis of Ag NWs and Ag/Ag$_2$S NWs in CO$_2$-saturated 0.5 M KHCO$_3$ at −0.95 V versus RHE. h) Δ(O/Ag) and i) ethanol FE of Ag NWs and Ag/Ag$_2$S NWs changed with time for which they got exposed under ambient conditions.

atomic emission spectrometer (ICP-AES). The catalyst loading was optimized to maximize both current density and mass activity (Figure S10, Supporting Information). Both Ag NWs and Ag/Ag$_2$S NWs exhibit enhanced mass activity and an increased onset potential upon transitioning from an Ar-saturated to a CO$_2$-saturated electrolyte, indicating that catalysts based on Ag NWs can effectively catalyze CO$_2$ electroreduction. The larger difference in mass activity between Ag NWs and Ag/Ag$_2$S NWs illustrates sulfurization of Ag NWs can greatly enhance the catalytic performance of CO$_2$ electroreduction. The mass activity of Ag/Ag$_2$S NWs is higher than that reported in the literature as well.[14,15] The voltammetry curves normalized by geometric area and estimated surface area of Ag exhibit consistent trends in the comparison of the activity in CO$_2$ electroreduction (Figure S11, Supporting Information). Therefore, the voltammetry curves show the excellent activity of Ag/Ag$_2$S NWs in CO$_2$ electroreduction.

The sulfurization of Ag NWs to improve the selectivity was further investigated systematically. There are three kinds of main products obtained from Ag NWs and Ag/Ag$_2$S NWs, which are hydrogen, carbon monoxide, and ethanol (Figure 2b). Among all the CO$_2$ electroreduction products, liquid products were of most interest and quantified in the liquid phase using ^{1}H nuclear magnetic resonance (^{1}HNMR) (Figure S12, Supporting Information), while the gas products were detected by gas chromatography (GC) (Figure S13, Supporting Information). The FE of formic acid detected in ^{1}HNMR was calculated as less than 2% and thus was not included in statistics. Our Ag NWs-based catalysts yield a single liquid-phase product with little interference from other alcohols or acids, which is rare with other catalysts.[16] Notably, sulfurization of Ag NWs promotes the production of ethanol and hinders hydrogen evolution reaction (HER) at each selected potential. For Ag NWs, the ethanol FE first increases and then decreases with the decreasing potential from

**ADVANCED
SCIENCE NEWS**

www.advancedsciencenews.com

**ADVANCED
MATERIALS**

www.advmat.de

−0.75 to −1.15 V versus RHE (reversible hydrogen electrode), reaching the ethanol FE of 25% at −0.95 V versus RHE. The highest CO FE of 55% is obtained at −0.95 V versus RHE, while hydrogen becomes the main product at −1.05 and −1.15 V versus RHE. After sulfurization of Ag NWs, the ethanol FE triples at −0.95 V versus RHE to 75%. For Ag/Ag$_2$S NWs, the ethanol FE was improved from 25% to 75% after sulfurization at −0.95 V versus RHE. The ethanol FE remains largely unchanged when the loadings of Ag/Ag$_2$S NWs are varied from 0.017 to 0.102 mg (Figure S14, Supporting Information), indicating that ethanol selectivity is independent of catalyst loading and likely determined by the local electronic structure and intermediate binding at the Ag/Ag$_2$S interface. Therefore, sulfurization of Ag NWs can greatly enhance the ethanol selectivity for CO$_2$ electroreduction.

Furthermore, the sulfurization degree can greatly influence the CO$_2$ electroreduction performance. The sulfurization degree was controlled by the concentration of Na$_2$S solution used from 1 to 100 mM. When the Na$_2$S concentration increased from 1 to 100 mM, the ethanol FE and partial current density ($j_{ethanol}$) first increased and then decreased, reaching a maximum when the Na$_2$S concentration is 10 mM (Figure 2c,d), which means Ag/Ag$_2$S interface formed via sulfurization can improve ethanol selectivity, as well as accelerate ethanol production kinetics driven by overpotential (Figure 2e). In fact, based on the analysis of the Tafel slope, the introduction of Ag$_2$S can reduce electrochemical reaction kinetics, reflecting a decrease in reaction rate (Figure S15, Supporting Information). When the sulfurization degree is too high (50–100 mM), the ethanol selectivity decreases because most of the surface is covered with Ag$_2$S, and the poorly conductive Ag$_2$S cannot participate in CO$_2$ electroreduction efficiently. The Ag/Ag$_2$S NWs are outstandingly competitive among both non-copper (Cu) catalysts and Cu-based catalysts (Figure 2f).[17–34] Therefore, appropriate sulfurization can improve the ethanol selectivity of Ag NWs for CO$_2$ electroreduction.

Besides the activity and selectivity, Ag/Ag$_2$S NWs can also improve the stability for CO$_2$ electroreduction. We investigated the stability of Ag NWs and Ag/Ag$_2$S NWs under operating conditions by long-term electrolysis, and Ag/Ag$_2$S NWs exhibit much higher stability of ethanol selectivity than Ag NWs (Figure 2g). In the long-term electrolysis, the current density of Ag NWs gradually increases with the competitive advantage of HER but the loss of ethanol selectivity (Figure S16, Supporting Information). Oppositely, Ag/Ag$_2$S NWs can maintain a stable current density and ethanol selectivity during 14 h (Figure 2g), along with the retention of Ag/Ag$_2$S heterointerface and Ag chemical state on Ag/Ag$_2$S NWs after CO$_2$ electroreduction (Figures S17,S18, Supporting Information), indicating the greater stability under operating condition. In addition, Ag-based nanomaterials are highly susceptible to oxidation under ambient conditions, and their ability to remain active under non-operating conditions is also an important performance indicator.[6] Variation of the atomic ratio (Δ) of O/Ag as determined by XPS shows that Ag NWs are more susceptible to oxidation when exposed to ambient conditions (Figure 2h). Ethanol selectivity of Ag NWs is completely lost in 20 days, while Ag/Ag$_2$S NWs yield a significant amount of ethanol over 20 days (Figure 2i), indicating greater stability under ambient conditions. TEM images of Ag/Ag$_2$S NWs with ambient exposure for 10 days exhibit the same morphological struc-

ture, confirming that the Ag/Ag$_2$S heterointerface remains morphologically intact (Figure S19, Supporting Information). Meanwhile, XPS spectra of Ag/Ag$_2$S NWs with different ambient exposure times reveal that the Ag 3d binding energy exhibits no obvious changes until 10 days, indicating the Ag electronic structure remains largely unchanged for 10 days. Only the Ag MNN Auger spectra can detect a slight difference after 10 days. (Figure S20, Supporting Information). Therefore, Ag/Ag$_2$S NWs can effectively enhance stability both under operating and ambient conditions.

2.3. Effect of Ag/Ag$_2$S Interface and Interfacial Electronic Structure

Ag/Ag$_2$S NWs with different sulfurization degrees were further investigated by XPS and electrochemical measurements to find out factors enhancing the ethanol selectivity. S/Ag atomic ratios on the surfaces of Ag NWs with different sulfurization degrees quantified by XPS (**Figure 3a**) increase with the Na$_2$S concentration and then remain constant after 10 mM. The binding energy of Ag3d (Figure 3b) first decreases and then increases with Na$_2$S concentration, reaching the lowest at 10 mM, which is consistent with the ethanol selectivity (Figure 2c). The shift to lower binding energy at a relatively low sulfurization degree is due to the higher Ag(I) proportion brought about by sulfurization.[35] Via the ratio of Ag area to electrochemical surface area (ECSA), we can quantify that the population of active Ag surface on Ag/Ag$_2$S NWs is ≈19% when Na$_2$S concentration is 10 mM (Figures S21,S22, and Table S2, Supporting Information). The shift to higher binding energy at a relatively high sulfurization degree is deduced to be caused by the adsorption of S$^{2−}$ on the surface of Ag$_2$S over a wide area. When sulfurization reaches a certain level, the remaining Ag surface no longer forms Ag$_2$S, and S$^{2−}$ is preferentially adsorbed on the Ag$_2$S surface. The limit of sulfurization on Ag NWs is also evidenced by the ratios of Ag area to ECSA, where Ag area/ECSA ratio for Ag NWs sulfurized by 100 mM Na$_2$S (0.12) is similar to that for Ag NWs sulfurized by 50 mM Na$_2$S (0.13), deviating from the expected decreasing trend observed at lower sulfurization degrees (Figure 3c; Table S2, Supporting Information). The exposed Ag and in situ grown Ag$_2$S form the Ag/Ag$_2$S interface. The importance of the Ag/Ag$_2$S interface is further emphasized by testing the CO$_2$ electroreduction activity of mechanically mixed Ag$_2$S NPs and Ag NWs (Ag$_2$S NPs × Ag NWs) (Figure 3d), which shares the same value of Ag area/ECSA with Ag/Ag$_2$S NWs (Table S2 and Figure S23, Supporting Information). The mixture of Ag$_2$S NPs and Ag NWs exhibits the same FE distribution of products with Ag NWs, implying the separate Ag$_2$S components do not contribute to the CO$_2$ electroreduction performance of Ag NWs. While Ag$_2$S NPs themselves cannot catalyze the conversion of CO$_2$ to ethanol during CO$_2$ electroreduction as well. Therefore, a properly exposed Ag/Ag$_2$S interface plays an important role in CO$_2$ electroreduction to ethanol.

Building on the critical role of the properly exposed Ag/Ag$_2$S interface in enhancing ethanol selectivity, the unique interfacial electronic structure of Ag/Ag$_2$S, driven by electron transfer effects, further improves the catalytic efficiency. UV–vis–NIR spectroscopy (Figure S24, Supporting Information) shows that separate Ag$_2$S component has significant absorption in the
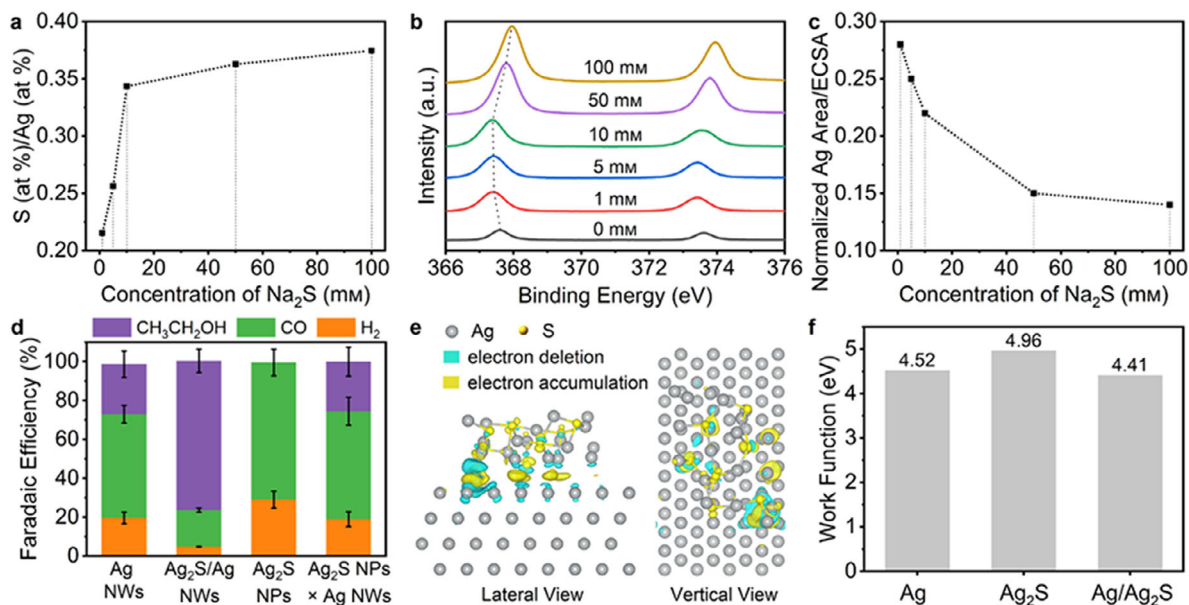
Figure 3. a) S/Ag ratios, b) XPS spectra for Ag3d, and c) normalized Ag area/ECSA of Ag NWs with different sulfurization degrees. d) FE of different products during CO_2 electroreduction on Ag NWs, Ag/Ag$_2$S NWs, Ag$_2$S NPs, and Ag$_2$S NPs × Ag NWs at −0.95 V versus RHE. e) Differential charge diagram of Ag/Ag$_2$S interface. f) Work functions of Ag, Ag$_2$S and Ag/Ag$_2$S.

near-infrared region (900–1000 nm) while Ag/Ag$_2$S NWs do not. Ag NWs mixed with Ag$_2$S NPs eliminates the possible interference of the strong surface plasmon resonance effect of Ag NWs on near-infrared absorption of Ag$_2$S, so this phenomenon is considered to be the cause of the unique interfacial electronic structure of Ag/Ag$_2$S brought by electron transfer effect.[36] The differential charge distribution after the combination of Ag and Ag$_2$S is illustrated in Figure 3e. A marked charge accumulation is observed at the interface of Ag/Ag$_2$S, indicating an electron-rich region. This suggests that the Ag/Ag$_2$S interface possesses enhanced catalytic activity, likely due to the increased availability of electrons for catalytic processes. The decrease in work function (Figure 3f; Figure S25, Supporting Information), calculated via DFT, further supports this finding. The work function of Ag/Ag$_2$S is calculated to be 4.41 eV, which is lower than 4.52 eV for Ag and 4.96 eV for Ag$_2$S, meaning electrons are more likely to be removed at the Ag/Ag$_2$S interface. The lower work function at the Ag/Ag$_2$S interface facilitates electron transfer, thereby boosting the catalytic efficiency of Ag/Ag$_2$S NWs in CO_2 electroreduction.[37] The Ag/Ag$_2$S interface is electron-rich and favors electron transfer during CO_2 electroreduction. Therefore, electrochemical measurements combined with XPS, UV–vis–NIR Spectroscopy, and DFT calculations prove that the Ag/Ag$_2$S interface is the main active site of Ag/Ag$_2$S NWs during CO_2 electroreduction to ethanol and the unique interfacial electronic structure promotes catalytic efficiency.

2.4. Mechanisms of Enhanced Ethanol Selectivity for CO_2 electroreduction

To investigate the molecular-level effects of sulfurization on CO_2 electroreduction, operando EC-SERS was employed to monitor intermediates formed during CO_2 electroreduction on Ag NWs

and Ag/Ag$_2$S NWs (**Figure 4a,b**). The Raman spectra obtained from Ag NWs provide insight into the fundamental catalytic processes of Ag-based catalysts (Figure 4a). Persistent peaks at 567 and 840 cm^{-1} are attributed to ν(Ag-OH) (ν, stretching vibration) and δ(AgO-H) (δ, bending vibration), respectively, indicating the stable adsorption of hydroxyl groups on Ag NWs in a CO_2-saturated 0.5 M KHCO$_3$.[38] The hydroxyl likely contributes to the creation of an alkaline catalytic interface, which may explain why Ag NWs demonstrate a certain efficiency in reducing CO_2 to ethanol.[39]

Beyond these peaks, several others are observed consistently from 0.05 to −0.95 V: 260, 356, 589, 692, 1007, and 1030 cm^{-1}, corresponding to Ag-CO frustrated rotation, ν(Ag-CO), δ(C-O), δ(Ag-CO$_3^{2-}$), $\nu_{symmetric}$(OCO), and $\nu_{asymmetric}$(OCO), respectively.[40–42] These peaks suggest that Ag NWs exhibit a preference for CO_2 electroreduction and demonstrate the capacity for CO_2 activation. The appearance of a peak at 1055 cm^{-1}, assigned to ν(C-O) of *COOH from −0.35 to −0.75 V, reflects the further reduction of activated CO_2.[43] As the potential decreases, the intensity of Ag-CO diminishes, while a new peak at 537 cm^{-1} emerges. Based on ^{13}C/^{12}C isotope exchange experiments (Figure 4c), this peak can be attributed to *CH$_2$CHO, a critical intermediate in ethanol formation.[43] Concurrently, the δ(OCO) peak shifts from 730 to 725 cm^{-1} as the potential decreases from 0.05 to −0.55 V.[41] With further reduction, no peaks are observed below 725 cm^{-1}. A new peak at 731 cm^{-1} emerges, shifting to 744 cm^{-1} at −0.95 V, which is assigned to δ(C-H) and appears alongside *CH$_2$CHO.[41] These signals elucidate the CO_2 electroreduction pathway leading to ethanol on Ag NWs. However, from 1270 to 2250 cm^{-1}, a prominent and persistent peak at 1761 cm^{-1} is attributed to the ν(O-C) stretch in formic acid.[44] The absence of the commonly observed *CO peak suggests that Ag exhibits weak adsorption of CO. Thus, operando EC-SERS not only provides a detailed understanding of the CO_2-to-ethanol catalytic process on Ag NWs
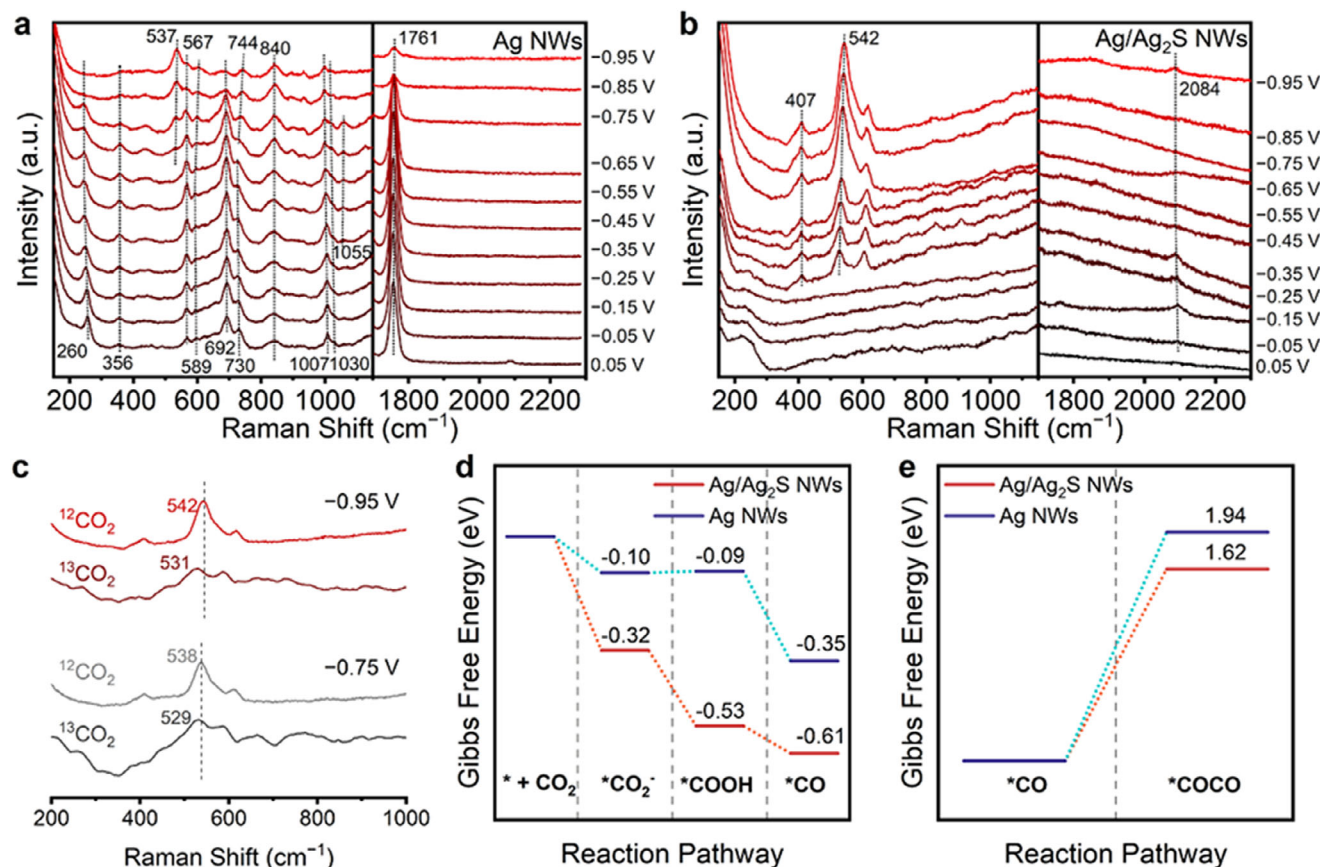
**ADVANCED
SCIENCE NEWS**

www.advancedsciencenews.com

**ADVANCED
MATERIALS**

www.advmat.de

Figure 4. SERS spectra of CO_2 electroreduction on a) Ag NWs and b) Ag/Ag_2S NWs at different potentials in CO_2-saturated 0.5 M $KHCO_3$. c) SERS spectra of CO_2 electroreduction on Ag/Ag_2S NWs at −0.75 and −0.95 V versus RHE in $^{12}CO_2$ and $^{13}CO_2$-saturated 0.5 M $KHCO_3$ solution. Gibbs free energy of d) CO_2 electroreduction to *CO and e) CO-CO coupling on Ag NWs and Ag/Ag_2S NWs.

but also highlights the limitations in ethanol production, stemming from weak CO adsorption and competition with formic acid formation.

In comparison to Ag NWs, Ag/Ag_2S NWs demonstrate enhanced ethanol selectivity during CO_2 electroreduction, as evidenced by the behavior of key carbonaceous intermediates (Figure 4b). The peak corresponding to *CH$_2$CHO at 542 cm^{-1} is more prominent over a broader potential range on Ag/Ag_2S NWs, indicating more efficient C-C coupling and an improved ability to facilitate ethanol formation. The appearance of *COOH in this potential range suggests that CO_2 from the bulk electrolyte diffuses to the catalyst surface, where it is activated and protonated. Simultaneously, the ν(C-O) stretch of *CO at 2084 cm^{-1} is observed on the Ag/Ag_2S NWs.[6] The sustained presence of peaks related to *COOH and *CO implies stronger *CO adsorption and higher *CO surface coverage on Ag/Ag_2S NWs, further enhancing its catalytic efficiency. Therefore, the enhanced ethanol selectivity on Ag/Ag_2S NWs is driven by efficient C-C coupling and *CO retention during CO_2 electroreduction.

DFT calculations also demonstrate that the high ethanol selectivity of Ag/Ag_2S NWs arises from a more favorable reaction pathway. The first step is the activation of adsorbed CO_2, forming $^*CO_2^-$, and then $^*CO_2^-$ couples with a proton to form *COOH

and the following intermediates. Energy barriers for these steps are lower on Ag/Ag_2S NWs, indicating the formation and protonation of $^*CO_2^-$ are easier at the Ag/Ag_2S interface (Figure 4d). The formation of CO on Ag NWs was calculated to be thermodynamically favorable as well although it is weaker, but *CO was detected only on Ag/Ag_2S NWs in SERS experiments. This error between DFT calculations and SERS experiments may be because of the surface concentration of *COOH.[6,28] The energy barrier of $^*CO_2^-$ protonation to *COOH was calculated to be much easier on Ag/Ag_2S NWs (−0.21 eV) than Ag NWs (0.01 eV), leading to the higher surface concentration of *COOH on Ag/Ag_2S NWs. As *CO formation is thermodynamically favorable, Ag/Ag_2S NWs with a higher surface concentration of *COOH can yield a higher *CO coverage, resulting in sufficiently strong *CO signals in SERS experiments.[6,28] Furthermore, CO-CO coupling is 1.94 eV on Ag NWs while 1.62 eV on Ag/Ag_2S NWs, indicating easier CO-CO coupling on Ag/Ag_2S NWs because of the lower energy barrier (Figure 4e). This corresponds with operando EC-SERS results that *CO and *CH$_2$CHO signals are persistent on Ag/Ag_2S NWs, while no obvious signals of these intermediates were detected on the Ag NWs (Figure 4a,b). Therefore, DFT calculations combined with SERS explain our experimental results well, showing why Ag/Ag_2S NWs exhibit high ethanol selectivity for CO_2 electroreduction.
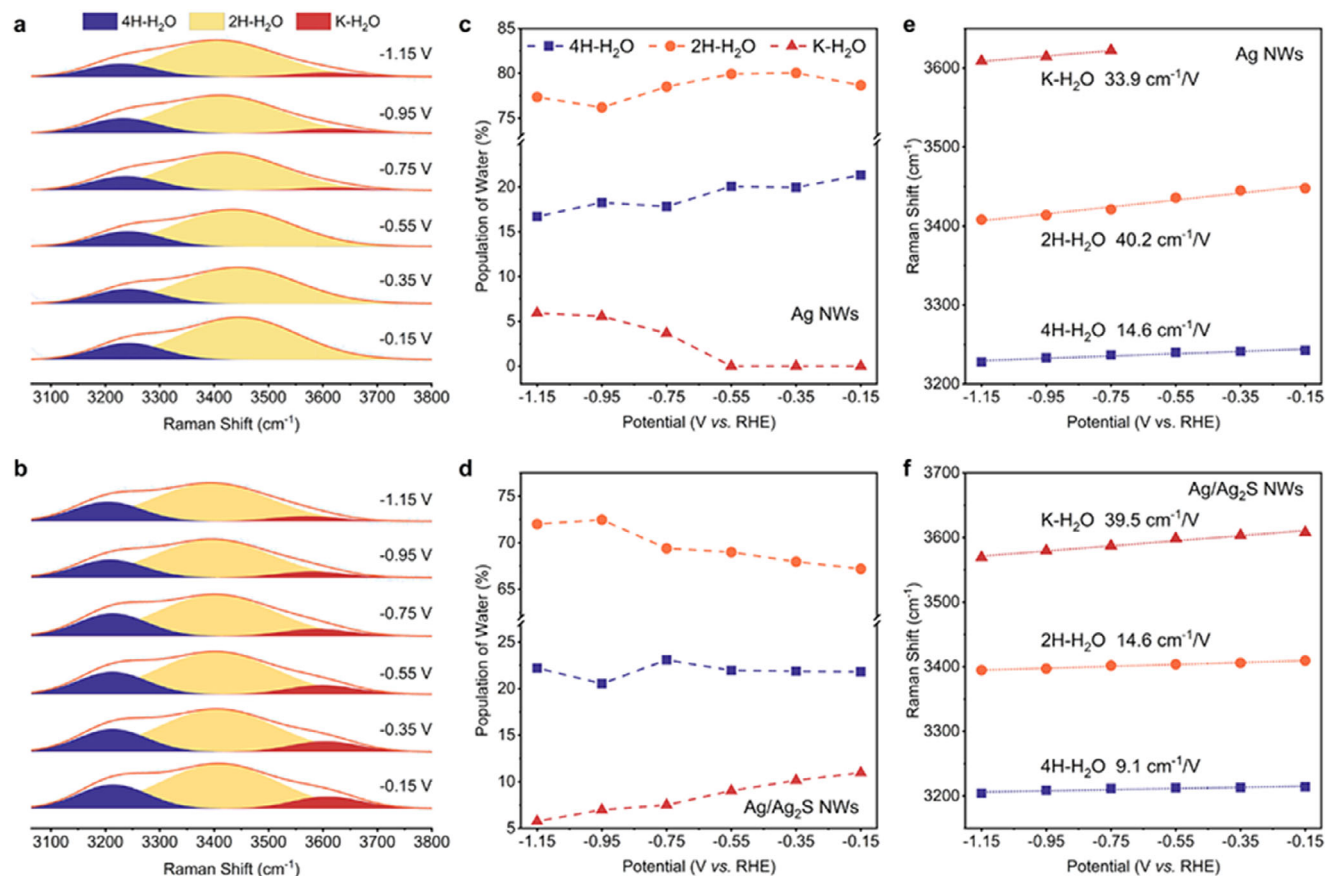
Figure 5. Gaussian fitted SERS spectra of O—H stretching vibrations on a) Ag NWs and b) Ag/Ag$_2$S NWs at different potentials in CO$_2$-saturated 0.5 M KHCO$_3$. The population of three types of O—H stretching on c) Ag NWs and d) Ag/Ag$_2$S NWs. The Raman shifts of O—H stretching vibrations on e) Ag NWs and f) Ag/Ag$_2$S NWs as a function of potential.

In addition to carbonaceous intermediates, investigation of interfacial water is crucial for understanding mechanisms underlying CO$_2$ electroreduction. Water, serving as a proton source in aqueous solution, plays a pivotal role in the protonation of intermediates. However, the detailed structure and its specific role in CO$_2$ electroreduction remain to be elucidated. To investigate these, the O-H stretching vibrations of water were detected by EC-SERS and analyzed through Gaussian fitting (**Figure 5a,b**; Figure S26 and Table S3, Supporting Information). From 3000 to 3800 cm^{-1}, three types of O—H stretching vibrations are identified: 4-coordinated hydrogen-bonded water (4H-H$_2$O, low wavenumber component), 2-coordinated hydrogen-bonded water (2H-H$_2$O, moderate wavenumber component) and K$^+$ coordinated water (K-H$_2$O, high wavenumber component).[10,45,46] The hydrogen bonding and cationic effects revealed by interfacial water structure provide valuable insights into how Ag/Ag$_2$S NWs enhance the activity and ethanol selectivity.

The role of hydrogen bonding in modulating HER is elucidated mainly through the behavior of 4H-H$_2$O and 2H-H$_2$O. The population of 4H-H$_2$O and 2H-H$_2$O on Ag NWs is higher compared to Ag/Ag$_2$S NWs (Figure 5c,d). This increased population is likely associated with the stable hydroxyls present, as evidenced by EC-SERS. These hydroxyls form a stable hydrogen bonding

network and inhibit CO$_2$ activation. Further analysis reveals that the Stark slope of 2H-H$_2$O on Ag NWs is higher than that of other water structures (Figure 5e), indicating the ν(O-H) of 2H-H$_2$O is more sensitive to the local electric field on Ag NWs.[47] In the hydrogen bonding network formed by surface hydroxyls and interfacial water, 2H-H$_2$O on Ag NWs, which is less stabilized by hydrogen bonding, more sensitive to the electric field, and more prone to forming the one-H-down structure,[45] is easier to be reduced. In comparison, 2H-H$_2$O on Ag/Ag$_2$S NWs occupies a lower proportion and is less sensitive than K-H$_2$O (Figure 5f), suggesting that the surface composition and structure of Ag/Ag$_2$S NWs influence the distribution and behavior of interfacial water in a way that reduces the activity of HER.

The presence of K-H$_2$O and interfacial K$^+$ concentration is critical for CO$_2$ electroreduction. On Ag NWs, K-H$_2$O emerges at potentials below −0.75 V (Figure 5c), which is attributed to the electrostatic migration of K$^+$ for charge compensation.[48] In contrast, K-H$_2$O is observed across a broader potential range on Ag/Ag$_2$S NWs. It is due to both the electrostatic migration and specific adsorption of cations driven by interfacial electric field strength brought by the negatively charged Ag$_2$S (Figures S27, Supporting Information). The elevated K$^+$ concentration on Ag/Ag$_2$S NWs leads to a competitive adsorption environment, where K$^+$ and protons compete for adsorption sites, further

facilitating CO_2 activation.[10,49] Moreover, K^+ plays a crucial role in facilitating C-C coupling by coordinating with the $^*CO + ^*CO$ intermediates near the catalyst surface. This coordination occurs as K^+ desolvates and partially replaces the hydrogen-bonding stabilization of interfacial water.[50] The highest Stark slope of K-H_2O on Ag/Ag_2S NWs indicates that K-H_2O induced by sulfurization responds more rapidly to an applied electric field, thereby facilitating its participation in the reaction and amplifying the K^+ effect. Computational results further reveal that the water adsorption and dissociation energies on Ag/Ag_2S NWs are lower than those on Ag NWs (Figure S28, Supporting Information), suggesting a more abundant proton supply and promoted protonation of intermediates. DFT calculations confirm that key intermediates, including $^*CO_2^-$, $^*COCO$, and $^*CHCHO$, are protonated more easily on Ag/Ag_2S NWs (Figure 4d), which is because of the lower adsorption and dissociation energies of water on Ag/Ag_2S NWs, leading to improved CO_2 reduction activity. Thus, the enhanced ethanol selectivity on Ag/Ag_2S NWs can be attributed to both the K^+ effect, which promotes CO_2 activation and C-C coupling, and the easier protonation of intermediates.

Operando EC-SERS and DFT calculations reveal the mechanism of enhanced ethanol selectivity on Ag/Ag_2S NWs. Operando EC-SERS detects $^*COOH$, $^*CO$ and $^*CH_2CHO$ on Ag/Ag_2S NWs, showing the high coverage of $^*CO$ and the high tendency for CO_2 to convert to ethanol. DFT calculations prove the reduced energy barriers of CO_2 activation, water dissociation, protonation, and C-C coupling by sulfurization. Analysis of interfacial water structures finds that the superior CO_2 electroreduction activity and higher ethanol selectivity of Ag/Ag_2S NWs come from the lower adsorption and dissociation energies of water on Ag/Ag_2S NWs, suppressed HER due to hydrogen bonding, along with easier protonation and C-C coupling is driven by K^+ effect.

3. Conclusion

In conclusion, interfacial water structures along with carbonaceous intermediates revealed the underlying mechanisms for enhanced ethanol selectivity and stability for CO_2 electroreduction on Ag/Ag_2S NWs. Optimized Ag/Ag_2S heterointerface from controlled sulfurization resulted in the unique electronic structure of the lowest Ag 3d binding energy as detected by XPS, which further provided the optimum adsorption sites for the intermediates and interfacial water to form ethanol. The ethanol FE of 75% at −0.95 V is achieved on such an optimum Ag/Ag_2S interface. Operando EC-SERS combined with DFT calculations proved that the enhanced ethanol selectivity originated from facilitated C-C coupling driven by high $^*CO$ coverage, lower energy barrier, and K^+ effect induced by sulfurization. Dynamic interfacial water behavior also accounts for lower adsorption and dissociation energies of water, suppressed HER, and easier protonation facilitating ethanol formation on Ag/ Ag_2S NWs. Therefore, operando EC-SERS combined with DFT calculations effectively explained the remarkable ethanol selectivity from Ag/Ag_2S NWs. This study not only establishes a rational atomic interface design for steering ethanol formation but also elucidates the dynamic interplay between catalyst electronic structure and interfacial species,

offering a molecular-level roadmap for advanced CO_2 conversion systems.

Conflict of Interest

The authors declare no conflict of interest.

Data Availability Statement

The data that support the findings of this study are available from the corresponding author upon reasonable request.

[1] P. De Luna, C. Hahn, D. Higgins, S. A. Jaffer, T. F. Jaramillo, E. H. Sargent, *Science* **2019**, *364*, 6438.

[2] Y.-G. C. Li, Z. Wang, T. Yuan, D.-H. Nam, M. Luo, J. Wicks, B. Chen, J. Li, F. Li, F. P. G. De Arquer, Y. Wang, C.-T. Dinh, O. Voznyy, D. Sinton, E H. Sargent, *J. Am. Chem. Soc.* **2019**, *141*, 8584.

[3] H. Shin, K. U. Hansen, F. Jiao, *Nat. Sustain.* **2021**, *4*, 911.

[4] X. Kong, J. Zhao, Z. Xu, Z. Wang, Y. Wu, Y. Shi, H. Li, C. Ma, J. Zeng, Z. Geng, *J. Am. Chem. Soc.* **2023**, *145*, 14903.

[5] X. Wang, Z. Jiang, P. Wang, Z. Chen, T. Sheng, Z. Wu, Y. Xiong, *Angew. Chem., Int. Ed.* **2023**, *62*, 202313646.

[6] Q. Liu, X.-G. Zhang, Z.-Y. Du, C.-J. Zou, H.-Y. Chen, Y. Zhao, J.-C. Dong, P.-P. Fang, J.-F. Li, *Sci. China Chem.* **2023**, *66*, 259.

[7] J. Yang, Q. Yu, H. Du, W. Zhang, Y. Zhang, J. Ge, H. Li, H. Li, H. Xu, *Adv. Sustain. Syst.* **2021**, *5*, 2100256.

[8] I. V. Chernyshova, P. Somasundaran, S. Ponnurangam, *Proc. Natl. Acad. Sci.* **2018**, *115*, E9261.

[9] C. Zhan, F. Dattila, C. Rettenmaier, A. Herzog, M. Herran, T. Wagner, F. Scholten, A. Bergmann, N. López, B. Roldan Cuenya, *Nat. Energy* **2024**, *9*, 1485.

[10] H. Liu, T. Yan, S. Tan, L. Sun, Z. Zhang, S. Hu, S.-H. Li, X. Kang, Y. Lei, L. Jiang, T. Hou, L. Liu, Q. Yu, B. Liu, *J. Am. Chem. Soc.* **2024**, *146*, 5333.

[11] Y. Wang, J. Zhang, J. Zhao, Y. Wei, S. Chen, H. Zhao, Y. Su, S. Ding, C. Xiao, *ACS Catal.* **2024**, *14*, 3457.

[12] Z. Liu, X. Lv, S. Kong, M. Liu, K. Liu, J. Zhang, B. Wu, Q. Zhang, Y. Tang, L. Qian, L. Zhang, G. Zheng, *Angew. Chem., Int. Ed.* **2023**, *62*, 2309319.

**ADVANCED
SCIENCE NEWS**

www.advancedsciencenews.com

**ADVANCED
MATERIALS**

www.advmat.de

[13] B. Tian, H. Wu, Y. Zhang, C. Chen, K. K. Abdalla, M. G. Sendeku, L. Zhou, J. Yu, Y. Wang, Y. Kuang, H. Xu, J. Li, X. Sun, *ACS Catal.* **2024**, *14*, 10904.

[14] D. Wang, L. Li, Q. Xia, S. Hong, L. Hao, A. W. Robertson, Z. Sun, *ACS Sustain. Chem. Eng.* **2022**, *10*, 11451.

[15] H. Guzmán, F. Salomone, S. Bensaid, M. Castellino, N. Russo, S. Hernández, *ACS Appl. Mater. Interfaces* **2022**, *14*, 517.

[16] J. Han, X. Bai, X. Xu, X. Bai, A. Husile, S. Zhang, L. Qi, J. Guan, *Chem. Sci.* **2024**, *15*, 7870.

[17] A. Singh, S. Barman, F. A. Rahimi, A. Dey, R. Jena, R. Kumar, N. Mathew, D. Bhattacharyya, T. K. Maji, *Energy Environ. Sci.* **2024**, *17*, 2315.

[18] Y. Meng, M. Li, Y. Xu, H. Liu, S. Kuang, S. Zhang, X. Ma, *Chem. Eng. J.* **2023**, *475*, 146456.

[19] F. Qi, K. Liu, D.-K. Ma, F. Cai, M. Liu, Q. Xu, W. Chen, C. Qi, D. Yang, S. Huang, *J. Mater. Chem. A* **2021**, *9*, 6790.

[20] Y. Liu, Y. Zhang, K. Cheng, X. Quan, X. Fan, Y. Su, S. Chen, H. Zhao, Y. Zhang, H. Yu, M. R. Hoffmann, *Angew. Chem., Int. Ed.* **2017**, *56*, 15607.

[21] Y. Song, S. Wang, W. Chen, S. Li, G. Feng, W. Wei, Y. Sun, *ChemSusChem* **2020**, *13*, 293.

[22] J. Qin, T. Wang, M. Zhai, C. Wu, Y. A. Liu, B. Yang, H. Yang, H. Wen, W. Hu, *Adv. Funct. Mater.* **2023**, *33*, 2300697.

[23] Q. Zhang, S. Tao, J. Du, A. He, Y. Yang, C. Tao, *J. Mater. Chem. A* **2020**, *8*, 8410.

[24] Z. H. Liu, H. Liu, M. L. Li, Y. C. Meng, X. Wang, T. X. Yan, Q. Fan, S. N. Lou, W. Q. Cui, S. Zhang, *ChemCatChem* **2024**, *16*, 2301700.

[25] F. Yang, C. Liang, H. Yu, Z. Zeng, Y. M. Lam, S. Deng, J. Wang, *Adv. Sci.* **2022**, *9*, 2202006.

[26] Q.-Y. Wang, Y-H. Li, Y. Zhao, Y.-Y. Chen, B.-J. Geng, R.-K. Ye, Q. Liu, X.-Q. Liu, Y.-X. Tong, Y.-J. Zhang, J. Cheng, P.-P. Fang, J.-F. Li, Z.-Q. Tian, *CCS Chem.* **2022**, *4*, 3319.

[27] J. Y. Kim, G. Kim, H. Won, I. Gereige, W.-B. Jung, H.-T Jung, *Adv. Mater.* **2022**, *34*, 2106028.

[28] C. Chen, Z. Sun, G. Qin, B. Wang, M. Liu, Q. Liang, X. Li, R. Pang, Y. Guo, Y. Li, W. Chen, *Adv. Mater.* **2024**, *36*, 2409797.

[29] H. Wang, X. Bi, Y. Yan, Y. Zhao, Z. Yang, H. Ning, M. Wu, *Adv. Funct. Mater.* **2023**, *33*, 2214946.

[30] T. Zhang, S. L. Xu, D. L. Chen, T. Luo, J. L. Zhou, L. C. Kong, J. J. Feng, J. Q. Lu, X. X. Weng, A. J. Wang, Z. Q. Li, Y. Q. Su, F. Yang, *Angew. Chem., Int. Ed.* **2024**, *63*, 2407748.

[31] B. Shao, D. Huang, R. K. Huang, X. L. He, Y. Luo, Y. L. Xiang, L. B. Jiang, M. Dong, S. X. Li, Z. Zhang, J. Huang, *Angew. Chem., Int. Ed.* **2024**, *63*, 2409270.

[32] S. Wang, F. Li, J. Zhao, Y. Zeng, Y. Li, Z.-Y. Lin, T.-J. Lee, S. Liu, X. Ren, W. Wang, Y. Chen, S.-F. Hung, Y.-R. Lu, Y. Cui, X. Yang, X. Li, Y. Huang, B. Liu, *Nat. Commun.* **2024**, *15*, 10247.

[33] X. Su, Z. Jiang, J. Zhou, H. Liu, D. Zhou, H. Shang, X. Ni, Z. Peng, F. Yang, W. Chen, Z. Qi, D. Wang, Y. Wang, *Nat. Commun.* **2022**, *13*, 1322.

[34] H. Xu, D. Rebollar, H. He, L. Chong, Y. Liu, C. Liu, C.-J. Sun, T. Li, J. V. Muntean, R. E. Winans, D.-J. Liu, T. Xu, *Nat. Energy* **2020**, *5*, 623.

[35] J. R. Ansari, N. Singh, S. Mohapatra, R. Ahmad, N. R. Saha, D. Chattopadhyay, M. Mukherjee, A. Datta, *Appl. Surf. Sci.* **2019**, *463*, 573.

[36] M. Sui, S. Kunwar, P. Pandey, J. Lee, *Sci. Rep.* **2019**, *9*, 16582.

[37] X. Luo, R. Jiang, Z. Ma, T. Yang, H. Liu, H. Deng, W. Wu, C. Dong, X.-W. Du, *Phys. Chem. Chem. Phys.* **2022**, *24*, 9188.

[38] E. R. Savinova, P. Kraft, B. Pettinger, K. Doblhofer, *J. Electroanal. Chem.* **1997**, *430*, 47.

[39] S. Garg, Q. Xu, A B. Moss, M. Mirolo, W. Deng, I. Chorkendorff, J. Drnec, B. Seger, *Energy Environ. Sci.* **2023**, *16*, 1631.

[40] C. Long, X. Liu, K. Wan, Y. Jiang, P. An, C. Yang, G. Wu, W. Wang, J. Guo, L. Li, K. Pang, Q. Li, C. Cui, S. Liu, T. Tan, Z. Tang, *Sci. Adv.* **2023**, *9*, adi6119.

[41] D. Bohra, I. Ledezma-Yanez, G. Li, W. De Jong, E A. Pidko, W A. Smith, *Angew. Chem., Int. Ed.* **2019**, *58*, 1345.

[42] W. Shan, R. Liu, H. Zhao, Z. He, Y. Lai, S. Li, G. He, J. Liu, *ACS Nano* **2020**, *14*, 11363.

[43] Y. Zhao, X.-G. Zhang, N. Bodappa, W.-M. Yang, Q. Liang, P M. Radjenovica, Y.-H. Wang, Y.-J. Zhang, J.-C. Dong, Z.-Q. Tian, J.-F. Li, *Energy Environ. Sci.* **2022**, *15*, 3968.

[44] D. Devasia, A. J. Wilson, J. Heo, V. Mohan, P. K. Jain, *Nat. Commun.* **2021**, *12*, 2612.

[45] Y.-H. Wang, S. Zheng, W.-M. Yang, R.-Y. Zhou, Q.-F. He, P. Radjenovic, J.-C. Dong, S. Li, J. Zheng, Z.-L. Yang, G. Attard, F. Pan, Z.-Q. Tian, J.-F. Li, *Nature* **2021**, *600*, 81.

[46] C.-Y. Li, M. Chen, S. Liu, X. Lu, J. Meng, J. Yan, H. D. Abruña, G. Feng, T. Lian, *Nat. Commun.* **2022**, *13*, 5330.

[47] D. Bhattacharyya, P. E. Videla, M. Cattaneo, V. S. Batista, T. Lian, C. P. Kubiak, *Chem. Sci.* **2021**, *12*, 10131.

[48] C.-Y. Li, J.-B. Le, Y.-H. Wang, S. Chen, Z.-L. Yang, J.-F. Li, J. Cheng, Z.-Q. Tian, *J. Am. Chem. Soc.* **2024**, *146*, 5242.

[49] X. Liu, M. T. M. Koper, *J. Am. Chem. Soc.* **2024**, *146*, 8.

[50] X. Yang, H. Ding, S. Li, S. Zheng, J.-F. Li, F. Pan, *J. Am. Chem. Soc.* **2024**, *146*, 5532.